Detection and analysis of oceanic thermal structures using NOAA AVHRR data

J. M. Cotos, J. Arias, A. Tobar

Department of Electronics and Computing Sciences, University of Santiago, Santiago de Compostela, Spain.

J. Galas

Institute of Applied Optics, ul. Kamionkowska 18, 03-000 Warszawa, Poland.

The NOAA series of polar satellites have proved highly useful for studying the ocean surface. In particular, the radiance information obtained through channels 4 and 5 of their Advanced Very High Resolution Radiometer (AVHRR), which are sensitive to radiation in the thermal infrared, allows sea surface temperature (SST) to be mapped with a precision of 0.1°C. This article describes the way this is done, and how such maps can be processed to study oceanic thermal structures and their variation. Particular attention is paid to the detection and monitoring of the upwelling of cold, nutrient-rich benthic waters from the ocean floor, since these areas constitute the richest fisheries.

1. NOAA satellites and signal reception

The polar-orbiting NOAA satellites (those now in service are NOAAs 9, 10 11 and 12) provide the best currently available satellite data on oceanic phenomena. Satellites with high spatial resolution, such as the LANDSAT series (spatial resolution 30 m per pixel) have very long periods (17 days in the case of LANDSAT), [1], making team useless for the study of faster-changing phenomena; while the meteorological satellite METEOSAT, for example, has excellent temporal resolution (48 infrared images of Europe per day), but a spatial resolution of only 5 km per pixel [2]. The balance struck between these extremes by the NOAA satellites, which have a spatial resolution of 1.1 km per pixel at the nadir and provide four images per day of any given area, is suitable for identification and monitoring of a number of important types of oceanic phenomena, including currents, thermal fronts, eddies and upwelling, all of which usually occupy several hundred square kilometers and generally vary on a time scale ranging from several hours to several days. The main NOAA image acquisition sensor is the five-channel Advanced Very High Resolution Radiometer. Current NOAA satellites also carry two other sensors allowing the construction of vertical profiles of atmospheric humidity and temperature: the High Infrared Radiation Sounder, which provides atmospheric radiometric and telemetric data, and the Microwave Sounding Unit, a passive microwave sensor operating at 5.5 μm [3].

1.1. AVHRR sensor

The wavebands to which the five AVHRR channels are sensitive are indicated on the atmospheric transmittance spectrum in Fig. 1 and listed in Tab. 1. Channels 1 and 2 respond to wavelengths in the visible region, channel 3 to the near infrared,
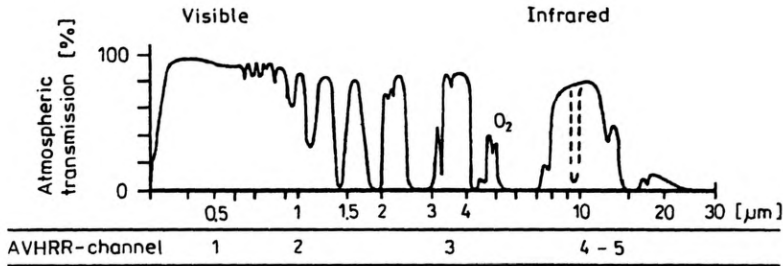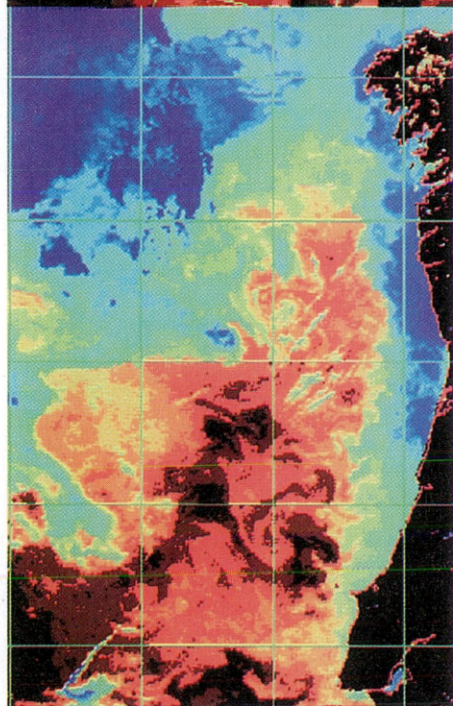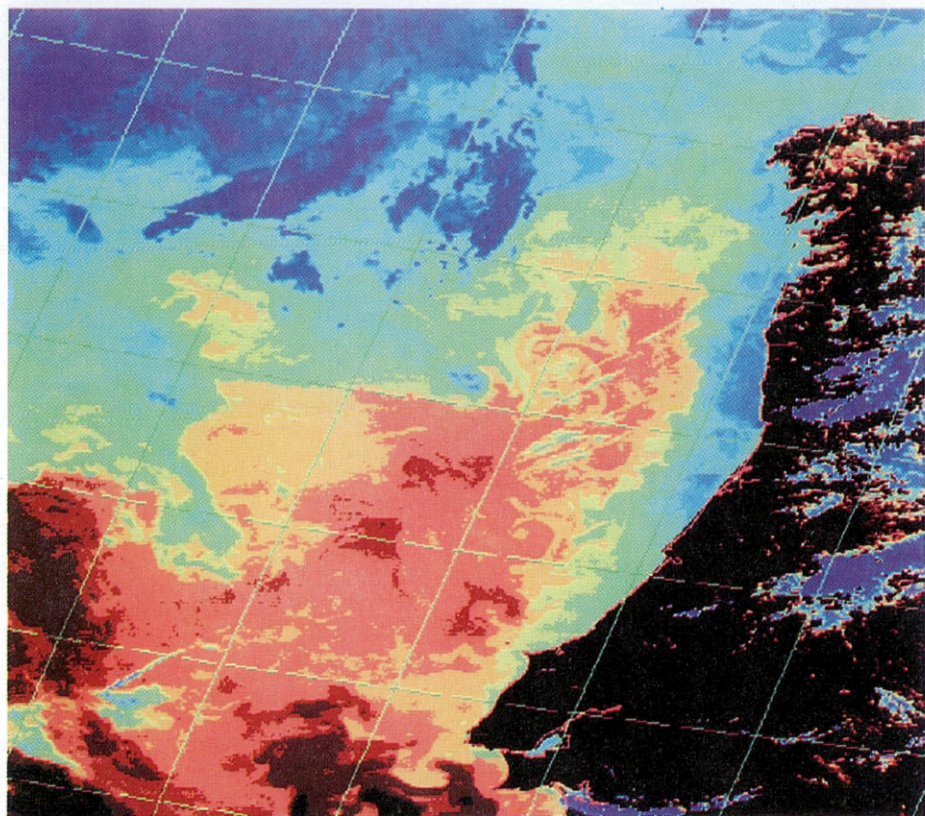

Fig. 1. Average atmospheric transssmision spectrum

Table 1. Bands covered by the channels of currently active NOAA satellites [µm]

NOAA	Channels				
	1	2	3	4	5
9 − 11 − 12	0.58 − 0.68	0.725 − 1.10	3.55 − 3.93	10.3 − 11.3	11.5 − 12.5
10	0.58 − 0.68	0.725 − 1.10	3.55 − 3.93	10.5 − 11.5	−

and channels 4 and 5 to adjacent bands in the thermal infrared . The width of each band is at most 1 µm, allowing highly accurate calculation of "brightness temperatures" from the radiances measured in each band.

1.2. Signal reception

Our satellite receiving station is equipped to receive analog and digital data directly from the geostationary satellites METEOSAT and GOES and from the polar-orbiting NOAA satellites. High resolution digital images are received from the NOAA satellites with a 2 metre parabolic antenna whose orientation is controlled by a PC-compatible personal computer. During each pass of the satellite (each takes about 15 min), the computer keeps the antenna pointing at the satellite using a file of ephemerides (TBUS) that is received daily from the NOAA agency by electronic mail. The received satellite data, which occupies rather more than 100 Mbytes (a 2000 × 5000 pixel, 10 bits per pixel image for each of the five AVHRR channels, plus scan-line headers and the data from the other sensors), is relayed to a Microvax II computer running under VMS, where its validity is checked. Valid data is passed via Ethernet to a server workstation, where it is stored on tape for subsequent processing by any of the users of the local network.

TOP: Image without
registration

BOTTOM: Image registrated
to rectangular
projection

Fig. 2. NOAA 11 AVHRR channel 4 image of the western coast of the Iberian Peninsula north of Lisbon on February 15th, 1993. Top: with a latitude-longitude grid overlaid. Bottom: transformed to rectangular projection

2. Signal processing

2.1. Preprocessing

For most purposes, the image obtained by a satellite is only useful if the geographical coordinates of its pixels are known. There are two widely used ways of calculating these coordinates. The first is to identify a number of unmistakable landmarks in the image, and use algorithms which create and apply an *ad hoc* transformation on the basis of the known coordinates of these landmarks. The second is to use the satellite ephemerides provided by the NOAA agency in TBUS to calculate a Keplerian orbit [4] for the satellite, and thence the coordinates of each pixel in the image. In our laboratory we use the second method. The upper image in Fig. 2 shows the western Iberian coast north of Lisbon as seen by NOAA 11 Channel 4 on February 15th, 1993, with conventional colouring and a superimposed latitude/longitude grid calculated as above. The lower image in Fig. 2 is the result of transforming the upper image to a standard map projection so as to facilitate comparison of maps produced at different times.

2.2. Brightness temperatures

The digitized sea surface radiance data received from a given satellite sensor channel allow calculation of the brightness temperature of the sea surface for that channel, *i.e.*, the temperature predicted by Planck's radiation distribution law without any allowance for the effects of the atmosphere on the radiation reaching the satellite sensor. Though the emissivity of the sea surface is practically unity and need not be corrected for in calculating brightness temperatures, it is necessary to take into account the non-linear response of the satellite sensor within each channel and the bias and scaling of the digitized data (Fig. 3).
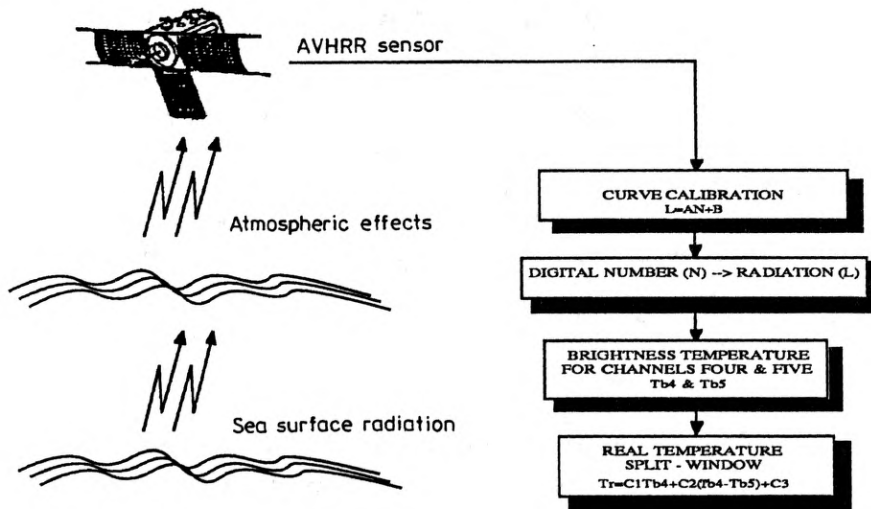

Fig. 3. Steps involved in the calculation of SST from remote sensing data

The non-linearity of the sensor response within a channel i centered on wavenumber k is taken into account with the help of a normalized response function supplied by the NOAA agency in the form of discrete values $\Phi(k_j)$ of the relative sensitivity of the sensor in n wavenumber intervals of widths $\Delta(k_j)$ into which the channel bandwidth is divided (for most channels $n = 60$). The normalization is such that

$$\sum_{j=0}^{n-1} \Phi(k_j)\Delta(k_j) = 1. \tag{1}$$

The radiance L_i perceived by channel i is thus given by

$$L_i = \sum_{j=0}^{n-1} B(k_j, T_{bi})\Phi(k_j)\Delta(k_j) \tag{2}$$

where T_{bi} is the corresponding brightness temperature and B is Planck's radiation distribution function

$$B(k, T_{bi}) = \frac{2\hbar c^2 k^3}{e^{\hbar ck/\varkappa T_{bi}} - 1}, \tag{3}$$

for radiation of wavenumber k from a body at temperature T radiating uniformly in all directions (in Eq. (3), k_B is Boltzmann constant, $\hbar$ — Planck constant and c — the speed of light).

Equation (2) is first used in the calculation of a calibration line allowing the bias and scaling of the digitized satellite data to be taken into account. A linear relationship is assumed to hold between L_i and the digitized data N_i for channel i

$$L_i = A_i N_i + B_i \tag{4}$$

where A_i and B_i are calculated from values of L_i and N_i for two reference objects of known temperature (deep space and a heated black-body cavity carried by the satellite) which are observed by the sensor during each scan. The values of N_i for the reference objects are received at the end of each scan line, and the corresponding values of L_i are calculated, using Eq. (2), from their known temperatures; the temperature of deep space is assumed to be 3 K, and that of the black-body cavity is obtained from end-of-scan data X_i from four platinum thermometers T_i $(i = 1-4)$ (specifically, the temperature of the black-body cavity T is calculated from

$$T_i = a_{i0} + a_{i1}X_i + a_{i2}X_i^2 + a_{i3}X_i^3 + a_{i4}X_i^4,$$

$$\bar{T} = \sum_{i=1}^{4} b_i T_i \tag{5}$$

where b_i and a_{ij} are the coefficients obtained pre-launch and supplied by the NOAA agency [3]). In the interests of stable calibration, X_i values are in practice averaged over 500 or so scan lines before being used in Eq. (5) (the software we have developed allows the exact number of lines in excess of 500 to be chosen by the user).

Once the calibration line (Eq. (4)) has been constructed, it can be used to calculate a value of L_i for each pixel from the corresponding value of N_i, and Eq. (2) can then
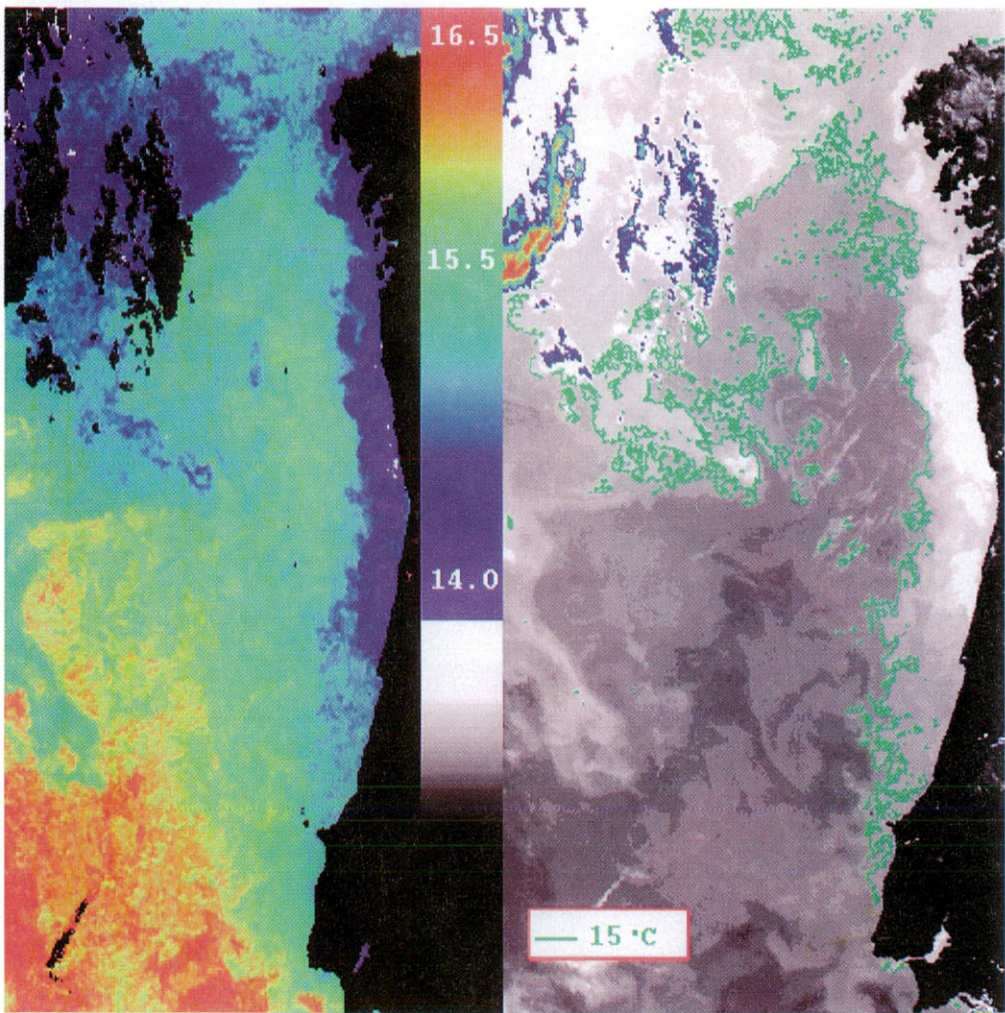
Fig. 4. HOAA AVHRR maps of the same area as in Fig. 2. Left: SSTs, with conventional colouring (see attached key). Right: grey-tone map of N_4 value (see text), with the 150C isotherm emphasized in green

Table 2. Calibration data used in Fig. 2

During Day

Algorithm	Channels	A	B	C
Split-window	4, 5	1.0351	3.046	−283.93

During night

Split-window	4, 5	1.0527	2.6272	−288.23
Dual-window	3, 4	1.0063	1.4544	−272.47

be used to obtain the corresponding brightness temperature (since exact calculation of T_{bi} from Eq. (2) is computationally demanding, the summation on the right-hand side is in practice replaced by a single term for a fixed wavelength in the region of flat sensor response).

Table 2 lists, for channels 3, 4 and 5, the reference object N_i values and the corresponding values of A_i and B_i that were obtained in constructing the SST map of Fig. 2.

2.3. Sea surface temperatures

The influence of the atmosphere on the radiation received by the satellite sensor is corrected for using the fact that the interference pattern is different for different radiometer channels. This circumstance has allowed the construction of empirical formulae for the calculation of true SSTs from brightness temperature data from a pair of sensor channels

$$SST = AT'_i + B(T'_i - T'_j) + C \tag{6}$$

where the pair (i, j) is either (4, 5) (the "split-window" equation, channels 4 and 5 being adjacent in the spectrum) or 3, 4 (the "dual-window" equation) [5]−[7]. Both variants may be used at night, but only the split window equation can be used in daytime, when channel 3 is blinded by sunlight reflected from the sea surface. Table 3 lists the empirical values of A, B and C for both equations under nighttime and (for the split window equation) daytime conditions.

Table 3. Coefficients for multispectral SST extraction (Eq. (6))

Channel	Slope	Intercept	Space gray level	Black-body gray level
3	−0.00150	1.14	989.4	669.6
4	−0.17932	178.08	993.1	420.4
5	−0.18270	182.12	996.8	354.0

The left-hand side of Figure 4 shows a typical SST map obtained as above, with conventional colour shading as indicated in the figure. Areas of land and cloud

have been blacked out after identification by means of unsupervised algorithms [8], [9] searching for appropriate combinations of infrared and visible radiation values (AVHRR channels 4 and 2). The right-hand side of Fig. 4 shows the corresponding map of channel 4 output (N_4 values) with cold sea shaded light, warmer sea dark and the 15°C SST isotherm superimposed in green; this isotherm (extracted from the SST data by a modified [10] Cluster Shade Edge Detection algorithm) [11] delimits the coastal region in which upwelling is occurring (see next section).

3. Upwelling

3.1. Physical origin, and biological and ecological significance

Due to the rotation of the Earth, trade winds blowing towards the equator off the western coasts of continental land masses casue seaward surface currents (Ekman currents) [12]. The water thus displaced from the coastal region is replaced by cold, dense, mineral-rich water welling up from the ocean depths (Fig. 5), the intensity of this upwelling depending to a large extent on the form of the continental shelf [13].
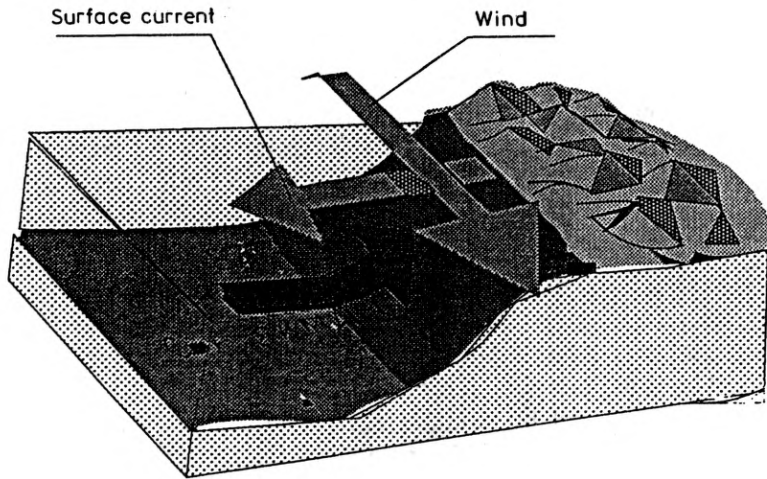

Fig. 5. Physics of upwelling

Upwelling is the main oceanic source of the basic nutrients underlying the food chain, and as such is associated with the world's major fisheries. Though areas of upwelling cover only about 1% of the oceanic surface, they provide about 50% of the world fishing catch. Because of this economic importance, considerable effort has been devoted to the study of upwelling by organizations such as the International Council of Exploitation of the Sea, the International Decade of Ocean Exploration and California Cooperative Fisheries (see, for example, the Coastal Upwelling Ecosystems Analysis project carried out by the IDOE in the 1970s) [14].

Ecologically, upwelling not only provides basic nutrients for phytoplankton, but may also act to regulate atmospheric CO_2, which is consumed by the phyto-

plankton: the intensification of the greenhouse effect by increasing atmospheric CO_2 levels strengthens the coastal winds responsible for upwelling, and hence increases upwelling and the consumption of CO_2 by the enlarged phytoplankton population. On the negative side, the low temperature of newly risen benthic waters leads to the water content of on-shore winds being partly lost at sea, which is why areas of upwelling are frequently associated with desert or semidesert regions on shore (including the Sahara, the Namibian Desert and the desert areas of California) [15].

3.2. Monitoring the movement of upwelling

SST maps do not remain constant during episodes of upwelling. The movement of temperature levels can be monitored by comparing SST maps constructed with an interval of one or two days (though in practice maps of N_4 values are more sensitive). The way we do this at our receiving station is related to a method based on the calculation of cross-correlation peaks between appropriately sized windows in the two images [16], [17]. The novelty of our modification of this strategy consists in the introduction of additional weighting to minimize the influence of pixels with rare N_4 values, which are assumed to be due to noise [17]. Specifically, our algorithm proceeds as follows.

Once land and cloud have been masked out of the two images (see subsection 3.3), the first image (minus a border 16 pixels wide) is divided into 32×32 pixel windows. An "overweighted cross-correlation function" C (based on a cross-correlation coefficient [18]), is then calculated for each window using the formula

$$C(d_x, d_y) = \frac{E[f(x,y)g(x+d_x,y+d_y)] - E[f(x,y)]E[g(x+d_x,y+d_y)]}{\sqrt{V[f(x,y)]\,V[g(x+d_x,y+d_y)]}} \qquad (7)$$

where $f(x,y)$ is the N_4 value of pixel (x,y) in the first image; $g(x+d_x, y+d_y)$ is the N_4 value of pixel $(x+d_x, y+d_y)$ in the second image (d_x and d_y range from -16 to $+16$);

$$E[t(x,y)] = \frac{1}{32 \times 32} \sum_{(x,y) \in W} t(x,y) P(t(x,y)) \qquad (8)$$

where W is the window being processed and $P(t)$ is the relative frequency of the value $t(x,y)$ in the whole of the image to which t refers; $E[f(x,y)g(x+d_x,y+d_y)]$ is similarly given by

$$E[f(x,y)g(x+d_x,y+d_y)] = \frac{1}{32 \times 32} \sum_{(x,y) \in W} f(x,y)g(x+d_x,y+d_y)P(g|f(x,y)) \qquad (9)$$

where $P(g|f(x,y))$ is the relative frequency of value $g(x+d_x,y+d_y)$ among those pixels $(x+d_x,y+d_y)$ of the second image for which the corresponding pixel (x,y) of the first image has value $f(x,y)$; and $V[t(x,y)]$ is given by

$$V[t(x,y)] = \frac{1}{32 \times 32} \sum_{(x,y) \in W} \{t(x,y) - E[t(x,y)]\} P(t(x,y)). \qquad (10)$$

The value of (d_x, d_y) for which $C(d_x, d_y)$ peaks is taken to be the displacement undergone, between the times of the first and second images, by the temperature levels present in the window being processed.

Figure 6 shows geometrically corrected NOAA 11 channel 4 images of the Atlantic Ocean off the coast of Galicia (N.W. Spain) on February 15th and 17th, 1993 (Figs. 6a and 6b, respectively). The coastline has been emphasized in green, and meridians and parallels have been superimposed at half-degree intervals. Figure 7 shows the results of subjecting the images of Fig. 6 to the method described in the previous paragraph; white dots show the centre of each 32×32 pixel window, and red-headed arrows the calculated displacements (white dots with no arrows correspond to areas of land or cloud). In the south there is a clear anticlockwise rotation of thermal masses around Vigo Seamount (a submarine peak located at a depth of 1000 m at 41.5 N 10.5 W), while nearer the coast the lack of east-west displacements reflects the stability of the area of the upwelling region.

3.3. Automatic detection of the upwelling

As is clear from Figures 4 and 6, upwelling is easily detected by eye in SST maps. However, as part of the development of an expert system for the detection and evaluation of broader classes of marine events, we have also carried out preliminary development of an image analysis routine for the automatic detection of upwelling. This routine calculates the first derivative of the N_4 profile along each of five parallels crossing our area of interest, and identifies sharp positive peaks in the derivative function as fronts separating warm sea to the west from cold sea to the east. Figure 8 shows the result of applying this routine to the 43rd parallel in the image of Fig. 6a; the large positive and negative peaks at the left of the derivative profile correspond to cloud borders, and would be masked out in the final, fully integrated version of our system.

4. Thermal fronts

When lines of constant temperature are extracted on SST maps it is frequently observed that in some places these lines are close making a horizontal gradient of temperature. When this phenomenon takes place it is called thermal front, and since this event is related with great amounts of fishes usually is also called fisher front.

Clark and Renard in 1966, used this formulae to obtain horizontal gradient SST and to get in this way the strongest fisher fronts

$$FT = -\frac{\partial}{\partial n}\left(\frac{\partial t}{\partial n}\right). \tag{11}$$

This way of detecting fronts consists in calculation of the points at which the second derivatives of SSTs with respect to the image coordinates become zero while the first derivatives are non-zero. This approach is illustrated in Fig. 9, which has been obtained from the SST data corresponding to Fig. 6a, and in which red
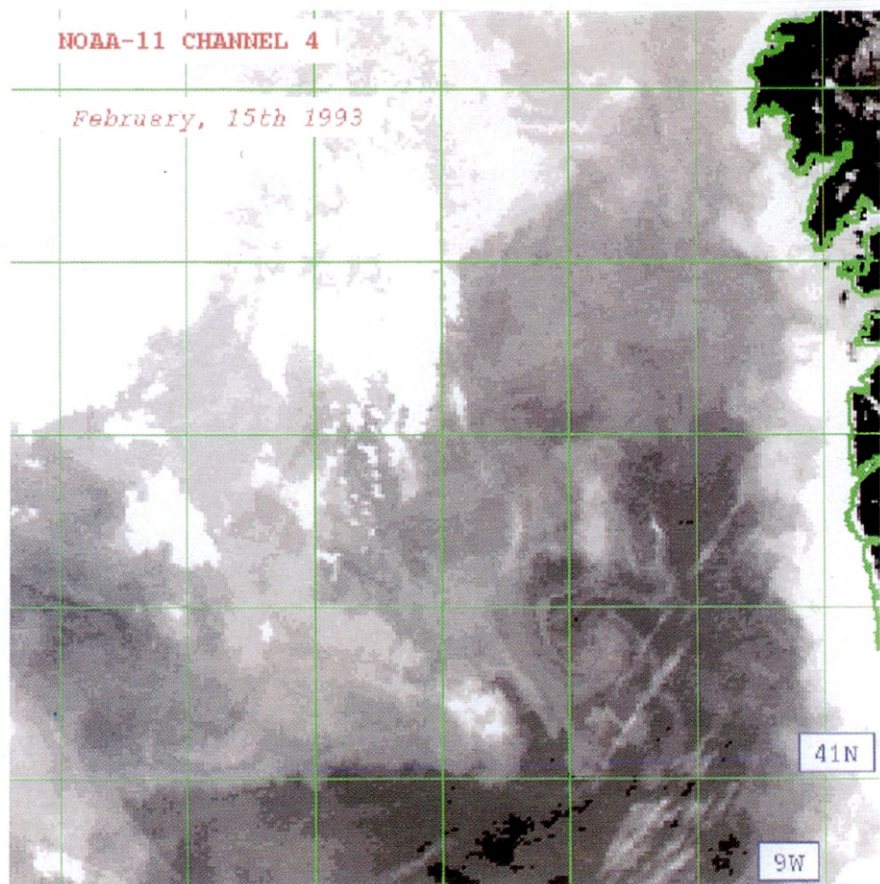
Fig. 6a. N_4 map of the Atlantic off Gallicia (N.W. Spain) on February 15, 1993
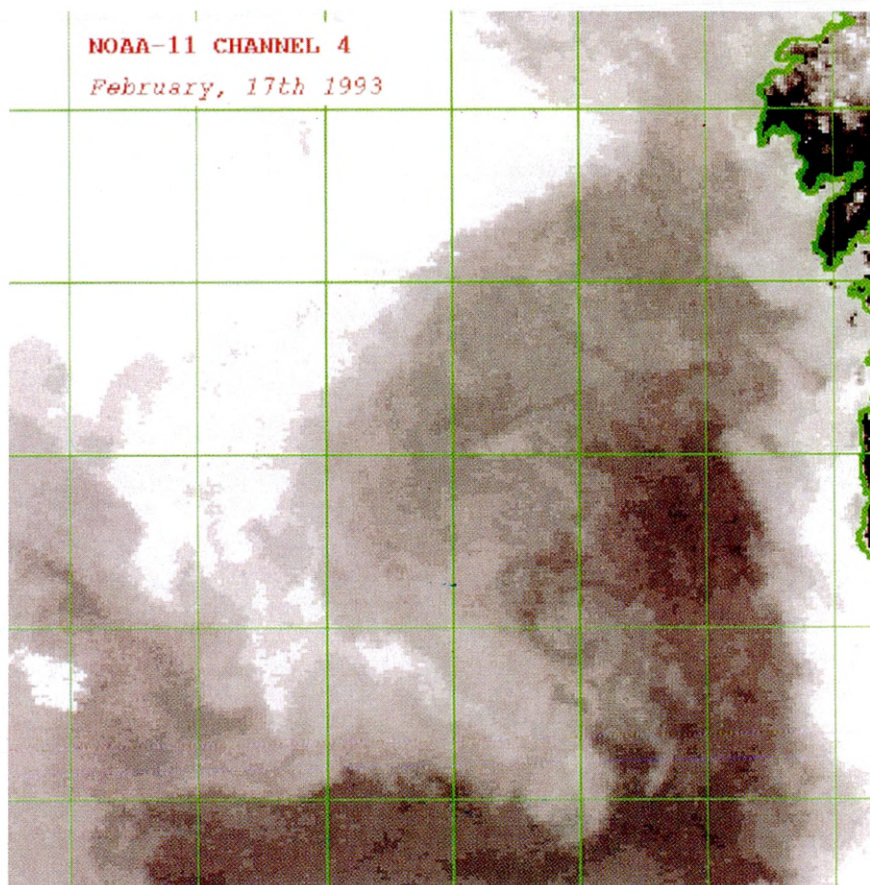
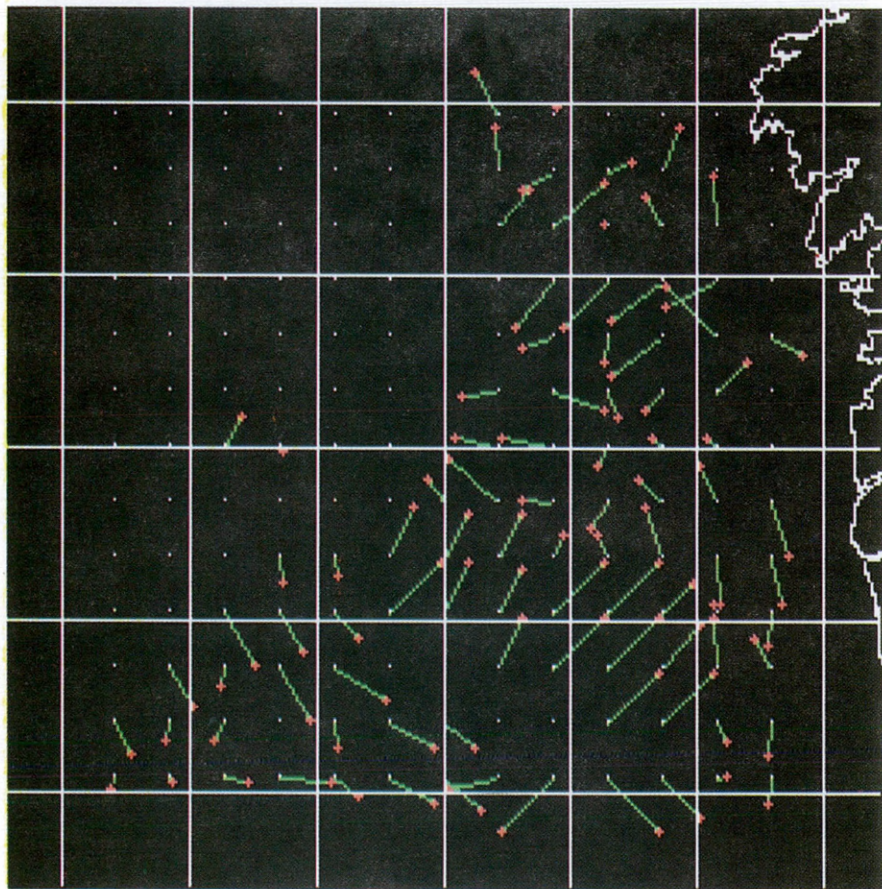Fig. 6b. N_4 map of the Atlantic off Gallicia (N.W. Spain) on February 17, 1993

Fig. 7. Thermal mass displacement calculated from the data of Figs. 6a and 6b
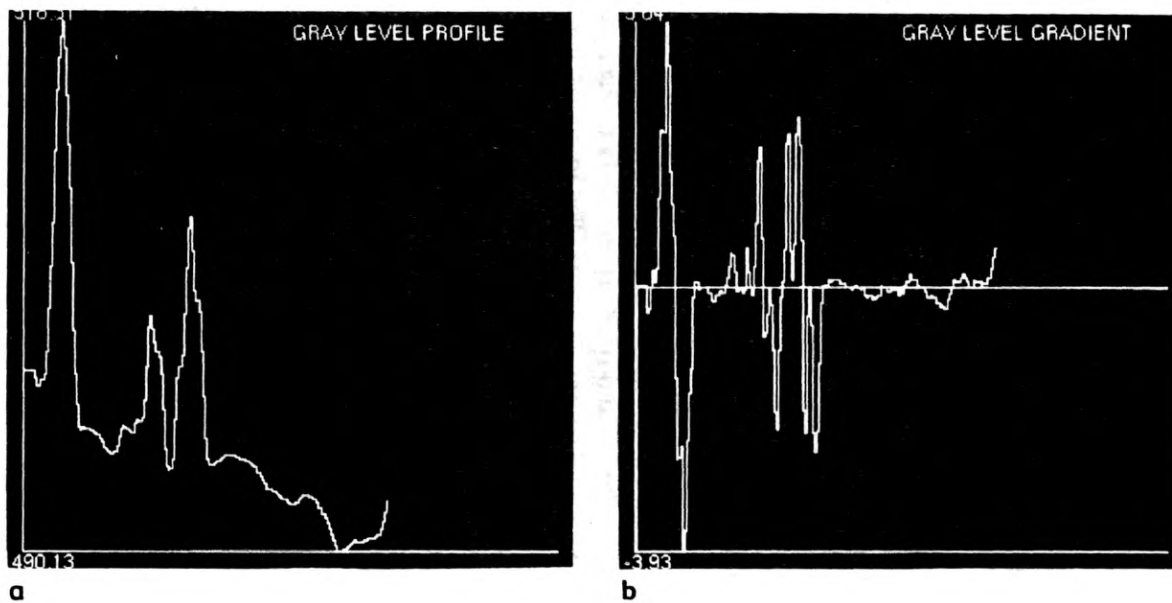
GRAY LEVEL PROFILE

GRAY LEVEL GRADIENT

a

b

Fig. 8. N₄ (a) and its first derivative (b) along the image line corresponding to latitude 43 N in Fig. 6a

contours indicate strong fronts (*i.e.*, those with large absolute values of the first derivative) and green contours weaker fronts.

Depending on which is original cause of the thermal front, we can classify them in three different classes:

1. Local fisfer fronts, originated by local meteorological conditions near islands, mouth of rivers, beaches, *etc.*

2. Thermal fronts associated to an isobaric divergence of surface winds near 500 − 300 millibars.

3. Advection currents of cold or dry air, or both together, usually making other kinds of thermal fronts.

We can consider the boundaries in the upwelling like a strong thermal front, with a very high economic relevance [19].

All of them are related because we can detect them in the same way as we have described above. The strong fronts in Fig. 9 show both the edge of the upwelling and the warm front advancing around Vigo Seamount.

4. Conclusions

The techniques described in this article make up most of the low-level tasks of the expert system mentioned earlier. We are currently carrying out trials in which information on isotherms and fronts is sent daily to the local offshore fishing fleet via INMARSAT communications satellites. The main catches of this fleet are tuna and sardine, the latter of which frequents the colder, zooplankton-rich upwelling areas while the former, a visual predator, prefers the less turbid warmer zones [20]. The information sent from our station improves the efficiency of the fleet by reducing fuel consumption and increasing the chances of good catches.

References

[1] MATHER D., *Computer Processing of Remotely-Sensed Images*, Wiley, New York 1987.
[2] BRIMACOMBE C. A., *Atlas of Meteosat Imagery*, ESA SP−1030, May 1981.
[3] LAURISTON L., NELSON G. J., PORTO F. W., *NOAA Technical Memorandum*, NESS 107, Washington D.C., 1979.
[4] CHUVIECO E., *Fundamentos de Teledetección Espacial*, Ediciones Rialp, Madrid 1990.
[5] MCCLAIN E. P., PICHEL W. G., WALTON C. G., J. Geophys. Res. **66** (1985), 11587.
[6] PRABHAKARA C., DALU G., KUNDE V. G., J. Geophys. Res. **79** (1974), 5039.
[7] ROBINSON I. S., *Satellite Oceanography*, [Ed.] Ellis Horwood Limited, Wiley, New York 1985.
[8] LILLESAND T. M., KIEFER R. W., *Remote Sensing and Image Interpretation*, Wiley, New York 1987.
[9] RICHARDS F. A., *Remote Sensing: Digital Image Analysis*, Springer−Verlag, 1986.
[10] COTOS J. M., TOBAR A., HERNÁNDEZ C., Revista de Teledetección, No. 1. 1993.
[11] HODYER R. J., PECKINPAUGH S. H., IEEE Trans. Geosci. Remote Sensing **27** (1989), 46.
[12] EKMAN V. W., Arch. Mat. Astronom. Fys. **2** (1905), 52.
[13] FIUZA A. F., [In] *Coastal Upwelling. Its Sediment Recording, Part a*, [Ed.] Plenum Press, New York 1983, p. 85.
[14] WOOSTER W. S., [In] *Coastal Upwelling*, American Geophysical Union, Washington 1981, p. 1.
[15] FRAGA F., *Coastal Upwelling in the West Coast of Spain*, Institute of Fisheries Resarch, Vigo, Spain, 1990 (personal communication).

Fig. 9. Thermal fronts in Fig. 6a, as calculated by the second derivative method. Strong fronts are shown in red, weaker fronts in green

[16] QING X. WU., PAIRMAN D., STEPHEN J. M., EDWARD J. B., IEEE Trans. Geosci. Remote Sensing **30** (1992), 166.

[17] EMERY W. J., THOMAS A. C., COLLINS M. J., J. Geophys. Res. **91** (1986), 12865.

[18] URKOWITZ H., *Signal Theory and Random Processes*, [Ed.] Artech House, 1983.

[19] BREAKER L. C., J. Marine Technol. Sci. **15** (1981), 32.

[20] FIELDER P. C., SMITH G. B., LAURS M., Marine Fisheries Rev. **3** (1984), 1.